



Eleven-year solar cycles over the last millennium revealed by radiocarbon in tree rings

Nicolas Brehm¹✉, Alex Bayliss², Marcus Christl¹✉, Hans-Arno Synal¹, Florian Adolphi^{3,4,5,13}, Jürg Beer⁶, Bernd Kromer⁷, Raimund Muscheler⁸, Sami K. Solanki^{8,9}, Ilya Usoskin^{10,11}, Niels Bleicher¹², Silvia Bollhalder¹, Cathy Tyers² and Lukas Wacker¹✉

The Sun provides the principal energy input into the Earth system and solar variability represents a significant external climate forcing. Although observations of solar activity (sunspots) cover only the last about 400 years, radionuclides produced by cosmic rays and stored in tree rings or ice cores serve as proxies for solar activity extending back thousands of years. However, the presence of weather-induced noise or low temporal resolution of long, precisely dated records hampers cosmogenic nuclide-based studies of short-term solar variability such as the 11-yr Schwabe cycle. Here we present a continuous, annually resolved atmospheric ¹⁴C concentration (fractionation-corrected ratio of ¹⁴CO₂ to CO₂) record reconstructed from absolutely dated tree rings covering nearly all of the last millennium (AD 969–1933). The high-resolution and precision ¹⁴C record reveals the presence of the Schwabe cycle over the entire time range. The record confirms the AD 993 solar energetic particle event and reveals two new candidates (AD 1052 and AD 1279), indicating that strong solar events that might be harmful to modern electronic systems probably occur more frequently than previously thought. In addition to showing decadal-scale solar variability over the last millennium, the high-temporal-resolution record of atmospheric radiocarbon also provides a useful benchmark for making radiocarbon dating more accurate over this interval.

Cosmogenic radionuclides are produced continuously in the Earth's atmosphere by highly energetic particles (cosmic rays)^{1,2}. Their atmospheric production rate depends on the galactic cosmic ray flux, the level of solar activity and the geomagnetic field strength^{3,4}. Solar activity can be parameterized by the solar modulation parameter Φ (in MeV) describing the solar magnetic shielding of galactic cosmic rays, which can be extracted from global cosmogenic nuclide production⁵. Cosmogenic radionuclides such as radiocarbon (¹⁴C) stored in tree rings or ¹⁰Be archived in ice cores are considered to be most reliable tools for solar activity reconstructions^{5–9}. However, a continuous, annually resolved and accurately dated record of ¹⁴C production spanning the era of sunspot observations and extending substantially further back in time has so far been missing.

We present a nearly 1,000-yr-long annually resolved and accurately dated record of atmospheric ¹⁴C concentration from trees covering multiple periods of high and low solar activity. Produced using state-of-the-art analytical techniques, it provides a benchmark for the most precise and temporally accurate reconstruction of ¹⁴C production that enables the systematic investigation of short-term solar variability, in particular the 11-yr Schwabe cycle, over the last millennium (AD 969–1933). It furthermore allows short ¹⁴C production events^{10–12}, which recently gained much attention because they were attributed to solar energetic particle (SEP) events^{13,14}, to be detected and studied. SEP events are a major concern for modern societies as they may cause severe damage to (extra-) terrestrial electronic

systems¹⁵. Last, but certainly not least, this annually resolved record of atmospheric ¹⁴C concentrations enables more reliable radiocarbon dating by substantially improving the radiocarbon calibration curve for the Northern Hemisphere¹⁶.

The presented record more than doubles the length of the longest existing annual resolution ¹⁴C record from the 1980s¹⁷. Although recently a number of discontinuous annually resolved ¹⁴C records over the last millennia^{18–25} have been presented, they are all of shorter length and some lack the required analytical precision (about 1.5‰) to allow a reliable and systematic study of short-term solar variability and SEP events²⁶.

Annual ¹⁴C record and ¹⁴C production over the last 1,000 yr State-of-the-art compact accelerator mass spectrometry²⁷ was applied to an absolutely dated tree ring archive producing 1,281 high-precision ¹⁴C measurements on tree rings from England and Switzerland that resulted in an almost 1,000-yr-long (AD 969–1933), annually resolved ¹⁴C record (Supplementary Section 1). The fine structure of the annual relative decay-corrected ¹⁴C concentration record ($\Delta^{14}\text{C}$ in Fig. 1a; see also Extended Data Figs. 1 and 2) agrees well with an existing but substantially shorter annual record of the University of Washington that spans the last 440 yr (QL, orange data in Fig. 1a)^{17,28,29}. However, a chi-squared analysis covering the full overlapping time period yields a $\chi^2 = 506$ ($N = 413$, $P = 0.0001$), indicating that the two records are significantly different based on a 95% confidence interval. The reason for this is an offset slowly evolving

¹Laboratory of Ion Beam Physics, ETHZ, Zurich, Switzerland. ²Historic England, London, UK. ³Department of Geology, Lund University, Lund, Sweden.

⁴Climate and Environmental Physics, University of Bern, Bern, Switzerland. ⁵Oeschger Centre for Climate Change Research, University of Bern, Bern, Switzerland. ⁶Eawag, Dübendorf, Switzerland. ⁷Institute of Environmental Physics, Heidelberg University, Heidelberg, Germany. ⁸Max-Planck-Institut für Sonnensystemforschung, Göttingen, Germany. ⁹School of Space Research, Kyung Hee University, Yongin, Republic of Korea. ¹⁰Space Physics and Astronomy Research Unit, University of Oulu, Oulu, Finland. ¹¹Sodankylä Geophysical Observatory, University of Oulu, Oulu, Finland. ¹²Underwater Archaeology and Dendroarchaeology, Office for Urbanism, Zurich, Switzerland. ¹³Present address: Alfred Wegener Institute, Helmholtz Centre for Polar and Marine Research, Bremerhaven, Germany. ✉e-mail: nbrehm@ethz.ch; mchristl@phys.ethz.ch; wacker@phys.ethz.ch

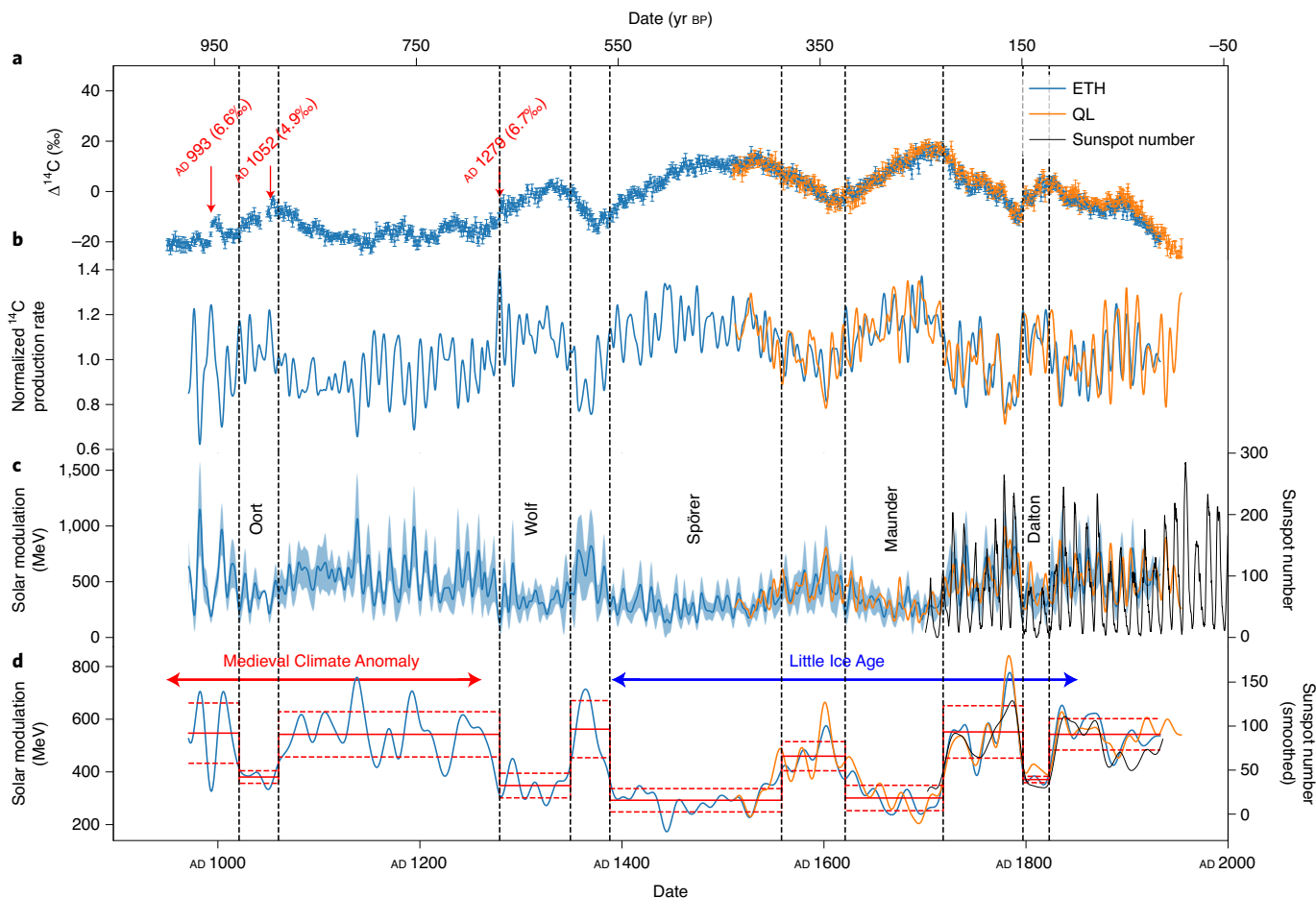


Fig. 1 | From annual $\Delta^{14}\text{C}$ records to solar modulation. **a**, Annual ETH and QL17 $\Delta^{14}\text{C}$ records with 2σ error bars. Red arrows indicate possible events, their respective date and $\Delta^{14}\text{C}$ increase. **b**, Normalized ^{14}C production rates calculated from ETH and QL data. **c**, Reconstructed solar modulation parameter Φ from ETH and QL ^{14}C production rates. The blue band indicates the uncertainty (in the ETH data) estimated by the Monte Carlo simulation. The international sunspot numbers³² (black, right y axis) are given for comparison. **d**, 20-yr low-pass-filtered Φ with mean values (ETH data, solid red lines) and the corresponding standard deviation (red dashed lines) for the different time periods. The 20-yr low-pass-filtered sunspot numbers (black, right y axis) are given for comparison. Vertical dashed black lines mark the beginnings and ends of grand solar minima.

between ETH and QL data beginning in AD 1850, which is probably caused by a regional imprint of the Suess effect (see Supplementary Section 2 for more detailed information). The Suess effect describes the dilution of atmospheric ^{14}C concentrations due to the combustion of radiocarbon dead fossil fuel commencing with the industrial revolution³⁰. This effect is more pronounced in our record because this time slice is covered by trees from England (Supplementary Section 1). When including only data before AD 1850 in the analysis, the resulting $\chi^2 = 347$ ($N = 329$, $P = 0.23$) indicates that the two subsets of data are indistinguishable within quoted uncertainties based on a 95% confidence interval (Supplementary Section 2).

Global ^{14}C production was reconstructed from the $\Delta^{14}\text{C}$ data (ETH and QL) using a carbon cycle box model (see ‘Modelling’ and Extended Data Figs. 3 and 4). Where $\Delta^{14}\text{C}$ denotes the decay-corrected $^{14}\text{C}/^{12}\text{C}$ ratio of a sample relative to a standard and normalized for isotope fractionation (in ‰). Production of ^{14}C varies by $\pm 25\%$ over the whole period in both records (Fig. 1b). The solar modulation parameter³¹ Φ was calculated from the ^{14}C production (see ‘Calculation of the solar modulation parameter’) derived from ETH and QL data. Both reconstructions of Φ correlate well with a Pearson correlation coefficient of 0.72, and they also agree well in phase over the 250-yr overlap with the international sunspot numbers³² (Fig. 1c; a more detailed depiction of the last 250 yr is given in Extended Data Fig. 5).

^{14}C production events

Recently, sharp increases in atmospheric ^{14}C were found in comparably short sequences of annually resolved tree ring data^{10–12} that were attributed to SEP events^{13,14}. Our continuous, annually resolved $\Delta^{14}\text{C}$ record reveals three rapid, event-like increases in atmospheric $\Delta^{14}\text{C}$ over the last 1,000 yr, which we define as a more than 4.5‰ rise in $\Delta^{14}\text{C}$ within 1 yr compared with the 4-yr average before and after the event (Fig. 1a). One of the increases is the previously identified AD 993 event, a SEP event¹⁴ that caused a tripling of the ^{14}C production for about 1 yr (see ‘Modelling of solar energetic particle events’ and Extended Data Fig. 6). Two other increases that could possibly represent SEP events occur around AD 1052 and AD 1279. In Fig. 2, the measured annual $\Delta^{14}\text{C}$ data around the two new event candidates are shown together with the fitted ^{14}C production spike and the resulting modelled atmospheric $\Delta^{14}\text{C}$. The AD 1052 event (Fig. 2a) is also detected by our model in two previously published datasets^{18,21}, whereas we could not reliably fit a production event to other ^{14}C datasets for the AD 1279 event candidate (Fig. 2b). This discrepancy is either the low precision of the Hong¹⁹ data or the large scatter of the Eastoe et al.¹⁸ record around the event. Still, the Eastoe et al. data¹⁸ indicate a higher level of $\Delta^{14}\text{C}$ after AD 1281. The calculated additional global ^{14}C production of the two new event candidates are $7.4 \pm 1.5 \text{ kg}$ ($\pm 1 \text{ s.d.}$) for the AD 1052 event

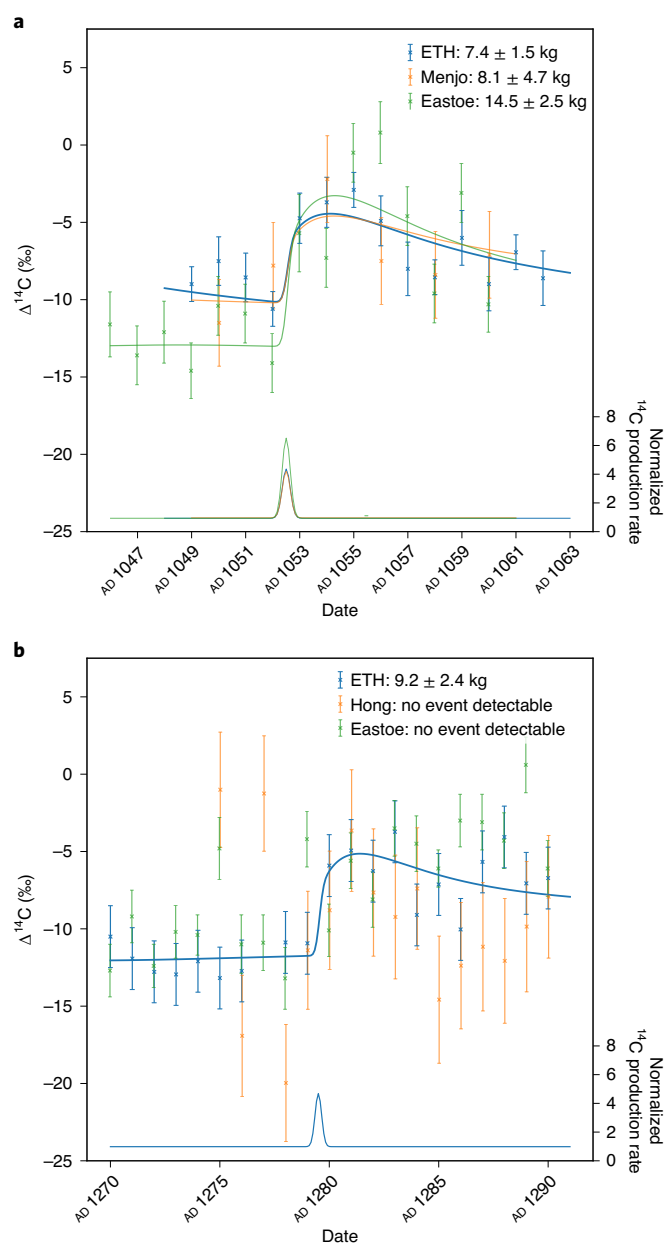


Fig. 2 | Two new event candidates detected in the 1,000-yr record.

a. The event at AD 1052. This event is confirmed by two previously published datasets (Menjo et al.²¹ and Eastoe et al.¹⁸). **b.** The event at AD 1279. This event is present only in the ETH data and not detectable in other datasets (Hong et al.¹⁹ and Eastoe et al.¹⁸). The error bars indicate the 2σ measurement uncertainty. The additional ^{14}C production of each respective event (given in the legends) is estimated by fitting a Gaussian ^{14}C production spike with a width of about two months (bottom part of **a** and **b**) to the data using our box model.

and 9.2 ± 2.4 kg for the AD 1279 event. With respect to global ^{14}C production, the two new event candidates are about 35% and 20% smaller, respectively, than the AD 993 event (11.3 ± 0.9 kg).

The presence of three candidate events in a continuous 1,000-yr record implies that they occur more frequently than previously thought, because so far only one event was known over approximately the last 1,000 yr. We observe a clustering of the events within the first 300 yr of the record, while we see no evidence for SEPs during the last 700 yr. We further note that the candidate events in AD 1052 and AD 1279 occurred during grand solar minima (Fig. 1b).

Table 1 | Grand solar minima and maxima as characterized by this study

	Time period	Φ (MeV)	Φ relative to reference (%)
Grand solar minima			
Oort	AD 1021–1060	390 ± 25	70 ± 5
Wolf	AD 1279–1349	350 ± 45	65 ± 10
Spörer	AD 1388–1558	290 ± 45	55 ± 10
Maunder	AD 1621–1718	300 ± 50	55 ± 10
Dalton	AD 1797–1823	370 ± 10	70 ± 5
Grand solar maxima			
Oort–Wolf	AD 1060–1279	545 ± 85	100 ± 15
Wolf–Spörer	AD 1349–1388	560 ± 110	100 ± 20
Spörer–Maunder	AD 1558–1621	460 ± 55	85 ± 10
Maunder–Dalton	AD 1718–1797	550 ± 100	100 ± 20
Dalton–AD 1930	AD 1823–1930	545 ± 60	100

The mean Φ is given with 1 s.d., and the last column shows modulation relative to the period after the Dalton minimum.

Long-term solar variability

The 20-yr low-pass-filtered reconstruction of Φ (Fig. 1d) shows a succession of distinct solar minima and maxima over the last 1,000 yr that agree well with the low-pass-filtered sunspot numbers. The periods of longer-lasting solar minima (that is, grand solar minima), defined by a combination of visual observations via sunspots and a ^{14}C reconstruction in the 1970s³³ or a more recent analysis of the low-resolution IntCal09 data³⁴ can now be more precisely characterized with respect to timing and amplitude (Fig. 1 and Table 1).

The average (± 1 s.d.) of the reconstructed Φ for the whole time period is 445 ± 135 MeV whereas a value of 545 ± 60 MeV is observed for the most recent period after the Dalton minimum (AD 1823–1930), which we choose as a reference (Table 1). Similar values for Φ are reconstructed during all strong solar maxima implying that (1) the reference period represents a strong solar maximum, and (2) over the entire 1,000-yr record, the average solar modulation was 20% weaker compared with the reference period. Furthermore, all known grand solar minima are clearly visible with a substantially lower Φ (55–70% of the reference; Table 1). The beginnings and ends of the grand solar minima were defined such that they coincide with minima in Φ (Fig. 1c and Table 1). Start and end points of a grand solar minimum were defined as the first minimum in solar modulation (Fig. 1c) after crossing a threshold of $\Phi = 400$ MeV in the 20-yr low-pass-filtered solar modulation record for more than 20 yr (Fig. 1d). The time frames of solar maxima were defined as the time intervals between minima.

The Oort solar minimum occurring between AD 1021 and AD 1060 (Fig. 1d) and the most recent Dalton minimum are substantially shorter and exhibit a higher level of solar activity than the other minima. We observe that the solar maximum between the Spörer and Maunder minima (AD 1558–1621) is notably weaker than the reference, with $\Phi = 460 \pm 55$ MeV (85% of the reference; Table 1). It seems that the Sun did not fully recover during this period that coincides with the Little Ice Age (AD 1400–1850, ref.³⁵; Fig. 1d). Our results show that during the Little Ice Age, solar modulation was continuously and substantially reduced by about 30% compared with the reference period with a mean Φ of 385 ± 125 MeV. This observation is corroborated by a recent reconstruction of Φ based on ^{10}Be in polar ice cores⁹, placing the absolute minimum of Φ over the last 2,000 yr within the Little Ice Age. We also observe a relatively high mean Φ of 525 ± 105 MeV for the time between AD 950 and AD 1250 coinciding with the Medieval Climate

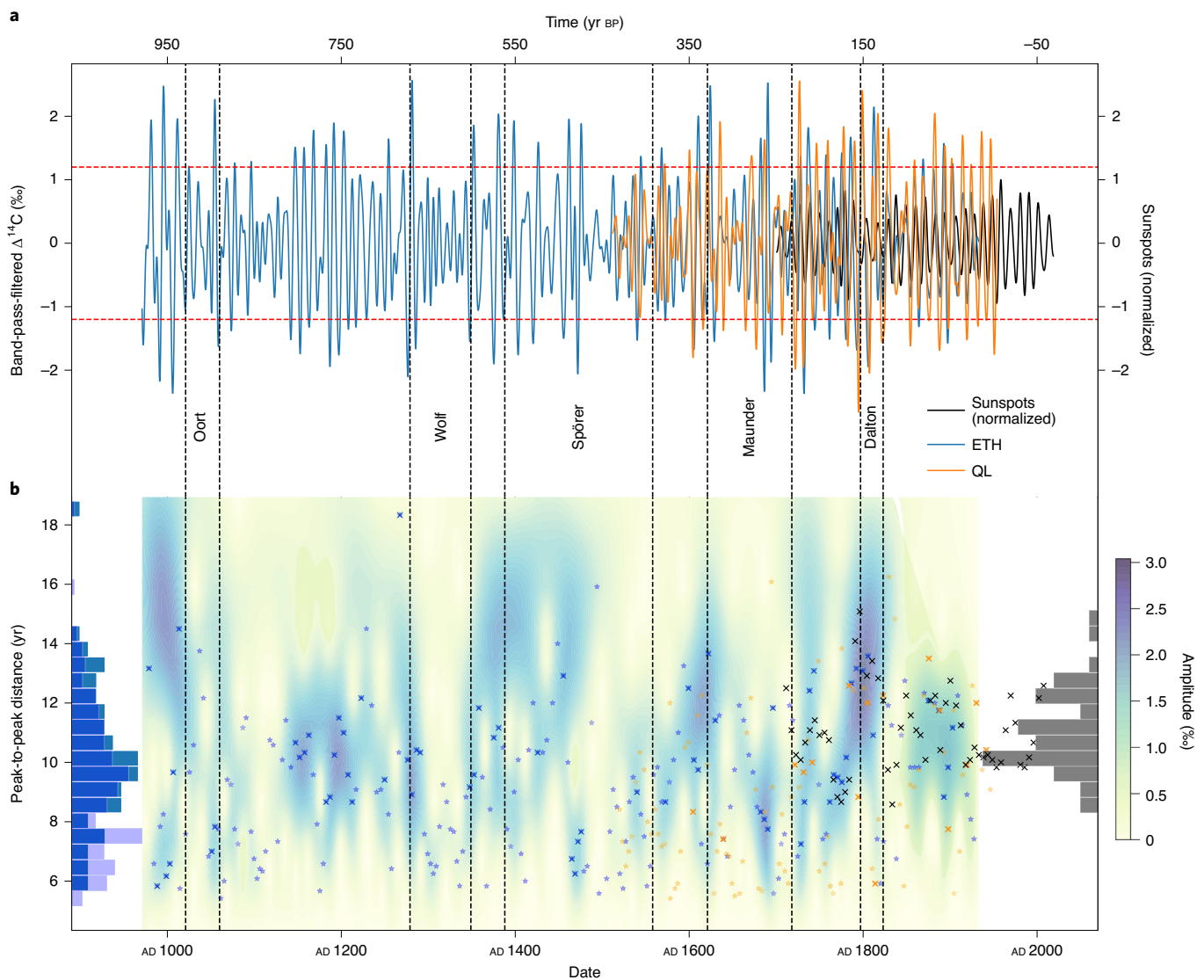


Fig. 3 | Frequency analysis of band-pass filtered $\Delta^{14}\text{C}$ records. **a**, 6- to 18-yr band-pass-filtered $\Delta^{14}\text{C}$ data and 1.2‰ significance level (red dashed lines). The band-pass-filtered and normalized sunspot record³² is shown in black. **b**, Morlet wavelet amplitude colour map of the band-pass-filtered ETH data. Data points indicate peak-to-peak distances of the band-pass-filtered $\Delta^{14}\text{C}$ records (light blue stars, ETH; light orange stars, QL; black crosses, sunspots). Blue and orange crosses mark the peak-to-peak distances for significant amplitudes (>1.2‰). The histograms on both sides show the distribution of period lengths for the sunspot numbers (black), all periods in the ETH data (light blue) and the significant periods only (dark blue). Vertical dashed black lines mark grand solar minima.

Anomaly (AD 950–1250; ref. ³⁶). A more detailed comparison of our high-resolution record of Φ with climate is beyond the scope of this study, and will be performed separately.

11-yr solar cycle over the last 1,000 yr

Unravelling fast solar oscillations from $\Delta^{14}\text{C}$ is challenging. For example, the amplitude of the 11-yr Schwabe cycle is expected to cause a change of only about 2‰ (ref. ¹⁷) in atmospheric $\Delta^{14}\text{C}$, whereas the average analytical uncertainty for a single measurement of the presented $\Delta^{14}\text{C}$ data is 1.8 ± 0.2 ‰. This complicates the analysis of short-term solar variability due to the difficulty of distinguishing between a real periodic signal and noise-induced, spurious periodicities³⁷.

To analyse the significance, length and amplitude of the Schwabe cycle in more detail, the $\Delta^{14}\text{C}$ records (QL and ETH data) and the sunspot record were 6- to 18-yr band-pass filtered (Fig. 3a) and the peak-to-peak distances of the minima (min.–min.) and maxima

(max.–max.) were evaluated (stars in Fig. 3b). In our analysis of the band-pass-filtered $\Delta^{14}\text{C}$ data, we estimate amplitudes greater than 1.2‰ as significant (2σ , red dashed line in Fig. 3), whereas smaller amplitudes may also be due to noise introduced by measurement uncertainties. The 1.2‰ limit was chosen such that for a random set of data with similar errors as our data, only 5% of the band-pass-filtered peaks are above this threshold. This indicates that smaller amplitudes, which are mainly present during grand solar minima, might be dominated by noise. For comparison, a wavelet transform was applied to the band-pass-filtered $\Delta^{14}\text{C}$ signal (ETH data, Fig. 3b). The bluish areas indicate amplitudes larger than about 1.2‰. Furthermore, a correlation of the significant peak-to-peak distances of the $\Delta^{14}\text{C}$ records (dark blue and dark orange crosses) with the observed sunspot number cycle length (black crosses in Fig. 3b) is observed. The above results show that atmospheric $\Delta^{14}\text{C}$ records carry the signal of short-term solar variability. However, the reconstruction of the Schwabe cycle for periods with small

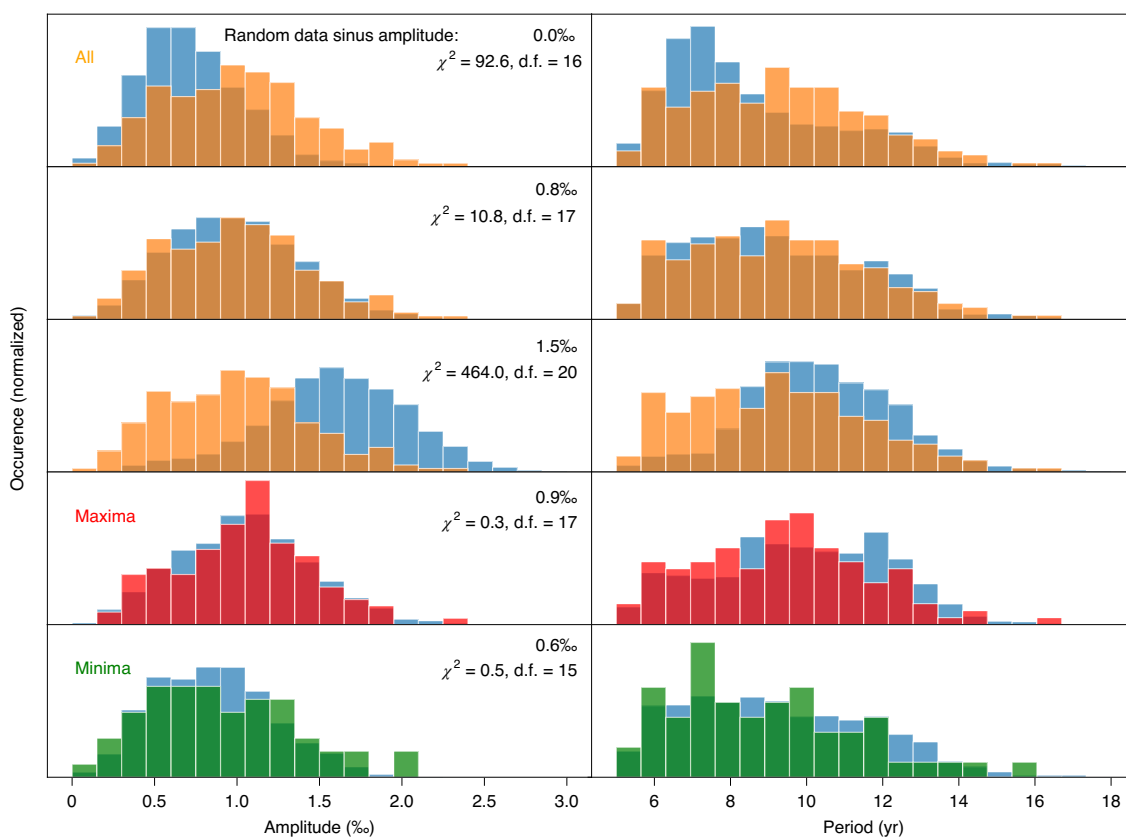


Fig. 4 | Amplitude and period distributions. Left: amplitude distributions. Right: period distributions. Normalized histograms of the full ETH $\Delta^{14}\text{C}$ record after 6- to 18-yr band-pass filtering are shown in orange. For the red (green) histograms, only data during solar maxima (minima) are used. The blue histograms show amplitude and period distributions (after band-pass filtering) of random data containing an artificial periodic 10.4 yr signal with different amplitudes. From top to bottom the amplitude of the artificial periodic signal was varied: 0‰ (white noise), 0.8‰ (best match with the full ETH data), 1.5‰ (strong solar cycle), 0.9‰ (best match during solar maxima) and 0.6‰ (best match during solar minima) (blue). A minimum χ^2 model was used to calculate the best fit with the artificial data.

amplitudes occurring during low solar activity is likely to be affected by noise, which in turn might cause apparently shorter period lengths.

The distribution of all peak-to-peak distances in the band-pass-filtered $\Delta^{14}\text{C}$ and sunspots record is shown in Fig. 3b ($\Delta^{14}\text{C}$: left y axis, blue; sunspots: right y axis, black). For $\Delta^{14}\text{C}$, the distributions of all (light blue) and only significant amplitudes (dark blue) are calculated separately. When only the significant peak-to-peak distances are considered (Fig. 3b, dark blue), the $\Delta^{14}\text{C}$ distribution is more similar to the distribution of sunspot periods (Fig. 3b, black, more details are given in ‘Random data generation’ and Extended Data Fig. 7). This again points to the presence of noise in the $\Delta^{14}\text{C}$ data that introduces high frequencies, shifting the distribution towards shorter peak-to-peak distances. We therefore conclude that the simple observation of shorter peak-to-peak distances during periods of low solar activity does not imply the presence of shorter solar cycles, but rather shows the increasing effect of noise introduced by the analytical uncertainties.

To demonstrate the significance and determine the period of the Schwabe cycle, we compare the observed periodicity and amplitude throughout the band-pass-filtered $\Delta^{14}\text{C}$ record with randomly generated test data that also contain a sinusoidal signal of variable periodicity (see ‘Random data generation’ and Extended Data Fig. 8). The amplitude of the sinusoidal signal is varied from 0 (pure noise) to 1.5‰ (strong Schwabe cycle), while the scatter of the random data is adjusted such that the artificial data show the same distribution of point-to-point distances as the measured $\Delta^{14}\text{C}$ data (see

‘Random data generation’). For the analysis, all datasets are 6- to 18-yr band-pass-filtered, and the distributions of peak-to-peak distances and amplitudes (Fig. 4, blue bars: artificial data, orange bars: measurements) were determined from the filtered data. The purely random dataset (no periodic signal) produces (false) periods with maximum occurrence between 6 and 8 yr and amplitudes around 0.6‰. Choosing an amplitude of 0.8‰ and a period of 10.4 yr for the sinusoidal signal for the artificial data produces the best match with the observations with respect to both period and amplitude distributions (Fig. 4). A χ^2 analysis using counting statistics for error estimation yields a χ^2 of 13.8 with 17 degrees of freedom, which is within a 95% confidence interval. From this we conclude that the 11-yr Schwabe cycle is present in the annually resolved $\Delta^{14}\text{C}$ record with an average amplitude of 0.8‰, which is substantially lower than reported previously¹⁷.

The amplitude of the 11-yr cycle might not have been constant over time. To investigate whether the amplitude of the Schwabe cycle depends on the overall level of solar activity, period and amplitude distributions were analysed separately during phases of low and high solar activity. Different patterns of the Schwabe cycle are observed during grand solar minima and maxima (red and green bars in Fig. 4), which are both significantly different from a purely random dataset (shown in Fig. 4 top). We obtained the best match to our data using an artificial dataset with a sinusoidal amplitude of 0.9‰ for high solar activity and 0.6‰ for low solar activity using a fixed frequency of $1/10.4\text{ yr}^{-1}$. The amplitude distribution of the data is substantially different from that with pure noise, especially

for periods of high solar activity. Although the individual measurement uncertainties are about 1.8‰ for single years, the results are statistically significant because we compare period and amplitude distributions over the long time period covered by the annually resolved $\Delta^{14}\text{C}$ record with about 10 data points per Schwabe cycle.

The continuous, nearly 1,000-yr-long record of annually resolved atmospheric $\Delta^{14}\text{C}$ from tree rings shows the persistence of the solar 11-yr Schwabe cycle through the last millennium. This builds on records based on the direct, visual, solar observations of sunspots on the Sun, which are only available for the last 400 years. The amplitude of the Schwabe cycle was found to correlate with the general level of the solar modulation with an amplitude of 0.6‰ (0.9‰) during solar minima (solar maxima). Successions of longer-lasting grand solar minima and solar maxima clearly stand out in our reconstruction and were (re-) defined with respect to both magnitude and timing.

The confirmation of the SEP event in AD 993 and the discovery of two new candidate events provides evidence that SEP events might occur irregularly and more often than previously thought. This finding is of considerable societal relevance because if such an event occurred today, it would probably be harmful to modern, often highly sensitive technological systems^{38,39}. The continuous ^{14}C record provides a unique tool with which to test and improve solar dynamo models, which have so far suffered from the relatively small number of recorded solar cycles. Improved solar models might eventually allow solar activity and SEP events to be predicted. Future annual records of ^{14}C measured in tree rings will probably extend much further back in time, providing improved statistical constraints on solar dynamo models, solar cycle length and amplitude, and their relation to climate.

Online content

Any methods, additional references, Nature Research reporting summaries, source data, extended data, supplementary information, acknowledgements, peer review information; details of author contributions and competing interests; and statements of data and code availability are available at <https://doi.org/10.1038/s41561-020-00674-0>.

Received: 6 December 2019; Accepted: 19 November 2020;

Published online: 04 January 2021

References

- Lal, D. & Peters, B. in *Kosmische Strahlung II: Handbuch der Physik* 551–612 (Springer, 1967).
- Herbst, K., Muscheler, R. & Heber, B. The new local interstellar spectra and their influence on the production rates of the cosmogenic radionuclides ^{10}Be and ^{14}C . *J. Geophys. Res. Space Phys.* **122**, 23–34 (2017).
- Kovaltsov, G. A., Mishev, A. & Usoskin, I. G. A new model of cosmogenic production of radiocarbon ^{14}C in the atmosphere. *Earth Planet. Sci. Lett.* **337**, 114–120 (2012).
- Snowball, I. & Muscheler, R. Palaeomagnetic intensity data: an Achilles heel of solar activity reconstructions. *Holocene* **17**, 851–859 (2007).
- Bard, E., Raisbeck, G., Yiou, F. & Jouzel, J. Solar irradiance during the last 1200 years based on cosmogenic nuclides. *Tellus B* **52**, 985–992 (2000).
- Muscheler, R. et al. Solar activity during the last 1000 yr inferred from radionuclide records. *Quat. Sci. Rev.* **26**, 82–97 (2007).
- Usoskin, I. G. A history of solar activity over millennia. *Living Rev. Sol. Phys.* **10**, 1 (2013).
- Beer, J., Vonmoos, M. & Muscheler, R. Solar variability over the past several millennia. *Space Sci. Rev.* **125**, 67–79 (2006).
- Steinhilber, F., Beer, J. & Fröhlich, C. Total solar irradiance during the Holocene. *Geophys. Res. Lett.* **36**, L19704 (2009).
- Miyake, F., Nagaya, K., Masuda, K. & Nakamura, T. A signature of cosmic-ray increase in AD 774–775 from tree rings in Japan. *Nature* **486**, 240–242 (2012).
- Miyake, F., Masuda, K. & Nakamura, T. Another rapid event in the carbon-14 content of tree rings. *Nat. Commun.* **4**, 1748 (2013).
- Park, J., Southon, J., Fahrni, S., Creasman, P. P. & Mewaldt, R. Relationship between solar activity and $\Delta^{14}\text{C}$ in AD 775, AD 994, and 660 BC. *Radiocarbon* **59**, 1147–1156 (2017).
- Usoskin, I. G. et al. The AD775 cosmic event revisited: the Sun is to blame. *Astron. Astrophys.* **552**, L3 (2013).
- Mekhaldi, F. et al. Multiradionuclide evidence for the solar origin of the cosmic-ray events of AD 774/5 and 993/4. *Nat. Commun.* **6**, 8611 (2015).
- Dyer, C., Hands, A., Ryden, K. & Lei, F. Extreme atmospheric radiation environments and single event effects. *IEEE Trans. Nucl. Sci.* **65**, 432–438 (2018).
- Bayliss, A. et al. Informing conservation: towards ^{14}C wiggle-matching of short tree-ring sequences from medieval buildings in England. *Radiocarbon* **59**, 985–1007 (2017).
- Stuiver, M. & Braziunas, T. F. Sun, ocean, climate and atmospheric $^{14}\text{CO}_2$: an evaluation of causal and spectral relationships. *Holocene* **3**, 289–305 (1993).
- Eastoe, C. J., Tucek, C. S. & Touchan, R. $\Delta^{14}\text{C}$ and $\delta^{13}\text{C}$ in annual tree-ring samples from sequoiadendron giganteum, AD 998–1510: solar cycles and climate. *Radiocarbon* **61**, 661–680 (2019).
- Hong, W. et al. Calibration curve from AD 1250 to AD 1650 by measurements of tree-rings grown on the Korean peninsula. *Nucl. Instrum. Methods Phys. Res. Sect. B* **294**, 435–439 (2013).
- Moriya, T. et al. A study of variation of the 11-yr solar cycle before the onset of the Spörer minimum based on annually measured ^{14}C content in tree rings. *Radiocarbon* **61**, 1749–1754 (2019).
- Menjo, H. et al. Possibility of the detection of past supernova explosion by radiocarbon measurement. In *Proc. 29th International Cosmic Ray Conference* (eds Sripathi Acharya, B. et al.) 357–360 (TIFR, 2005).
- Miyahara, H. et al. Variation of solar activity from the Spörer to the Maunder minima indicated by radiocarbon content in tree-rings. *Adv. Space Res.* **40**, 1060–1063 (2007).
- Miyahara, H. et al. Transition of solar cycle length in association with the occurrence of grand solar minima indicated by radiocarbon content in tree-rings. *Quat. Geochronol.* **3**, 208–212 (2008).
- Fogtmann-Schulz, A. et al. Variations in solar activity across the Spörer minimum based on radiocarbon in Danish oak. *Geophys. Res. Lett.* **46**, 8617–8623 (2019).
- Kudsk, S. G. K. et al. New single-year radiocarbon measurements based on Danish oak covering the periods AD 692–790 and 966–1057. *Radiocarbon* **62**, 969–987 (2019).
- Usoskin, I. G. et al. Revisited reference solar proton event of 23 February 1956: assessment of the cosmogenic-isotope method sensitivity to extreme solar events. *J. Geophys. Res. Space Physics* **125**, e2020JA027921 (2020).
- Synal, H. A. & Wacker, L. AMS measurement technique after 30 years: possibilities and limitations of low energy systems. *Nucl. Instrum. Methods Phys. Res. Sect. B* **268**, 701–707 (2010).
- Stuiver, M. Solar variability and climatic-change during the current millennium. *Nature* **286**, 868–871 (1980).
- Stuiver, M. & Quay, P. D. Atmospheric ^{14}C changes resulting from fossil-fuel CO_2 release and cosmic-ray flux variability. *Earth Planet. Sci. Lett.* **53**, 349–362 (1981).
- Keeling, C. D. The Suess effect: ^{13}C - ^{14}C interrelations. *Environ. Int.* **2**, 229–300 (1979).
- Gleeson, L. J. & Axford, W. I. Solar modulation of galactic cosmic rays. *Astrophys. J.* **154**, 1011–1026 (1968).
- Sunspot Index and Long-term Solar Observations* (SILSO WDC, 2019); <http://www.sidc.be/silso/>
- Eddy, J. A. The Maunder minimum. *Science* **192**, 1189–1202 (1976).
- Usoskin, I. G., Solanki, S. K. & Kovaltsov, G. A. Grand minima of solar activity during the last millennia. *Proc. Int. Astron. Union* **286**, 372–382 (2012).
- Brönnimann, S. et al. Last phase of the little ice age forced by volcanic eruptions. *Nat. Geosci.* **12**, 650–656 (2019).
- Goosse, H., JoelGuioit, Mann, M. E., Dubinkina, S. & Sallaz-Damaz, Y. The medieval climate anomaly in Europe: comparison of the summer and annual mean signals in two reconstructions and in simulations with data assimilation. *Glob. Planet. Change* **84–85**, 35–47 (2012).
- Ganopolski, A. & Rahmstorf, S. Abrupt glacial climate changes due to stochastic resonance. *Phys. Rev. Lett.* **88**, 038501 (2002).
- National Research Council *Severe Space Weather Events—Understanding Societal and Economic Impacts: A Workshop Report: Extended Summary* (National Academies, 2009).
- Schrimpf, R. D. & Fleetwood, D. M. *Radiation Effects and Soft Errors in Integrated Circuits and Electronic Devices* (World Scientific, 2004).

Publisher's note Springer Nature remains neutral with regard to jurisdictional claims in published maps and institutional affiliations.

© The Author(s), under exclusive licence to Springer Nature Limited 2021

Methods

Sample preparation and quality control. Our study focuses on the reconstruction of the past ¹⁴C/¹²C levels in the atmosphere from accurately dated tree ring chronologies^{40,41}. Dendrochronologically dated trees represent the most reliable archive for the reconstruction of past atmospheric ¹⁴C/¹²C ratios⁴² and therefore are considered to be the most suitable for a temporally accurate reconstruction of solar activity at the highest possible (that is, annual) resolution.

Dendrochronologically dated wood samples from England, supplied by Historic England, and from Switzerland, supplied by the laboratory for dendrochronology of the city of Zurich, were dissected into annually resolved samples weighing 30–60 mg (Supplementary Section 1). Typically, 54 tree ring samples with 4 wood blanks (2 Brown Coal (BCB) and 2 Kauri Stage 7 (K7B)) and two AD 1515 reference samples⁴³ each weighing 30–60 mg, were prepared in 15 ml glass test tubes together in a batch (making 60 in total). In a slightly modified procedure following Némec et al.⁴⁴, samples were first soaked in 5 ml 1 M NaOH overnight at 70 °C in an oven. Then the samples were treated with 1 M HCl and 1 M NaOH for 1 h each at 70 °C in a heat block, before being bleached at a pH of 2–3 with 0.35 M NaClO, at 70 °C for 2 h. The remaining white holo-cellulose was then freeze-dried overnight.

About 2.5 mg dried holo-cellulose was wrapped in cleaned Al capsules⁴⁵ and converted to graphite using the automated graphitization line AGE⁴⁶. A sample batch for accelerator mass spectrometry measurements consisting of 39 samples each was made up of three oxalic acid 1 (OX1) and four oxalic acid 2 (OX2) standards, 26 samples, two cellulose blanks, two chemical blanks and two AD 1515 reference samples (individual cellulose preparations of the AD 1515 reference were used for at least two measurement sets). Two accelerator mass spectrometry sample batches were typically prepared within a week and subsequently measured. Data analysis was performed with the ETH Zurich in-house data reduction software BATS⁴⁷. Typically, a 1% external error for sampling and sample preparation was added to the finally reported uncertainties. Duplicate graphite samples were prepared and measured from about one-third of the prepared cellulose samples for quality control, resulting in 304 of at least doubly measured samples with a χ^2 of 300, which is well within a 95% confidence interval. In addition, full repeats from different trees were in good agreement with our uncertainty estimates.

Two internal wood reference materials from AD 1515 (pine and oak) and two different radiocarbon free wood blanks (K7B and BCB from Reichwalde) were repetitively analysed together with the annual wood samples. Whereas the wood blanks were used for blank subtraction in the data evaluation process, the AD 1515 references were used for quality control only (Supplementary Section 2).

Processing blanks samples typically yielded radiocarbon ages between 48 and 52 kyr without any background correction (see also Sookdeo et al.⁴³). The results given for the AD 1515 reference are very consistent (Supplementary Fig. 2) with a mean radiocarbon age of 344.2 ± 1.0 yr BP (F¹⁴C: 0.95805 ± 0.00014, where F¹⁴C denotes the measured ¹⁴C to ¹²C ratio of the sample divided by the measured ¹⁴C to ¹²C ratio of the standard⁴⁸). The sample scatter of 11 yr is slightly less than the mean uncertainty of 14 yr given by the applied data reduction ($\chi^2 = 76$, $n = 124$) (ref.⁴³). A similar result was obtained for the cellulose repetition, where the agreement of the individual measurements was also slightly better than expected from the estimated uncertainties.

Our uncertainties of typically 14 yr are somewhat smaller than the 17 yr for the annual measurements reported in IntCal13 for this period⁴² for the last 440 yr BP after the application of an uncertainty multiplier of 1.3 on the original data^{49,50}.

Comparison with other datasets. The new annual measurements are in good agreement with the raw values of IntCal13⁴², although measured at a higher temporal resolution for the first 60% of the record. However, we see some statistically significant (> 2 σ) offset towards older ages for short periods of time (Extended Data Fig. 1). The most significant offset of 19.5 ± 1.4 yr is observed after AD 1850. IntCal13 is here based on (mostly) annual measurements on a tree from the coastal region of the pacific from the northwest United States and from Alaska^{17,51,52}. Although the reason for this offset is unknown, we can only speculate about possible regional offsets at the beginning of industrialization in England, or about laboratory offsets due to applying different measurement procedures. The direct comparison between the QL data and our data gives a χ^2 of 469, with 413 degrees of freedom yielding a *P* value of 0.97, implying that the ETH data are significantly different from the QL data. But if the last 100 years are neglected in the comparison, and only the data older than AD 1850 are compared, we get a χ^2 value of 321, with 329 degrees of freedom, giving a *P* value of 0.38, which is well within a 95% confidence interval.

When we compare the Jordanian Juniper samples from the Levante region (AD 1685–1950)⁵³ with our new dataset, we see that the strong offsets they observed compared with IntCal13 are greatly reduced (Extended Data Fig. 2) and we consequently question the interpretation of variable and strong regional offsets⁴⁹. A significant offset of about 20 yr is observed between 270 and 200 yr BP when comparing our new dataset with the annual raw data of IntCal13. While we can only speculate whether the Suess effect starting in the middle of the nineteenth century may be responsible for the observed discrepancy, it is presently unclear why the ¹⁴C signal in the trees from the northwest United States is different to the European trees and why Alaskan trees, in contrast, agree so well with European trees.

For further comparison of the reconstructed solar modulation parameter with sunspot numbers, a zoomed version of Fig. 1c is shown in Extended Data Fig. 5. We can see that most of the solar cycles can accurately be reconstructed with the ETH data, as well as with the QL data. For time periods where the band-pass-filtered signal of the QL data has a significant amplitude of 1.2% or higher, we get a Pearson correlation coefficient (with ETH data) of 0.52, whereas for time periods of smaller amplitudes, the correlation coefficient is only 0.07. Over the whole overlapping time span, a Pearson correlation coefficient of 0.29 was obtained between the band-pass-filtered datasets. We note, however, that the relation between sunspots and Φ is indirect, via the open solar magnetic flux, which is not only a nonlinear relation⁵⁴, but may also vary substantially in the relative phase⁵⁵. Thus, a linear comparison between sunspot number and Φ (for example, by calculating the Pearson correlation coefficient) is not very informative. To compare the results of peak-to-peak distances directly with sunspots, we compared the results for both the QL data and ETH data with the peak-to-peak distances of the sunspots over the overlapping time period. The result is shown in Extended Data Fig. 7. We can see that the significant (>1.2%) peak-to-peak distances give a similar distribution to the sunspots.

Modelling. An improved carbon box model based on the model of Gütler et al.⁵⁶ was used to model the carbon cycle (Extended Data Fig. 3). Their model uses 11 boxes to simulate the exchange between the global atmosphere, biosphere and oceans. To model the Northern and Southern Hemisphere separately, our model was extended to 22 boxes (11 boxes for each hemisphere). The carbon content of each box is distributed according to the respective relative carbon reservoir masses of the corresponding hemisphere. Radiocarbon is produced in the stratosphere and the troposphere of both hemispheres: 70% is produced in the stratosphere and 30% in the troposphere. The fluxes were adjusted to ensure a correct Δ^{14} C offset between the northern and southern troposphere.

The ¹²C and ¹⁴C contents of each box after a time step are calculated with

$$\begin{aligned} N_i^{12}(t + \Delta t) &= N_i^{12}(t) + dN_i^{12}(t)\Delta t \\ N_i^{14}(t + \Delta t) &= N_i^{14}(t) + dN_i^{14}(t)\Delta t \\ dN_i^{12}(t) &= \sum_j F_{ji}^{12}(t) - \sum_j F_{ij}^{12}(t) \\ dN_i^{14}(t) &= -\lambda N_i + \sum_j F_{ji}^{14}(t) - \sum_j F_{ij}^{14}(t) + P_i(t) + P_{st,i} \end{aligned}$$

Here $N_i^{12,14}$ is the ^{12,14}C content of each box in gigatonnes and λ is the decay constant of ¹⁴C. The time step Δt was chosen to be one month for all the following simulations. The ¹⁴C and ¹²C fluxes are given by the following:

$$F_{ij}^{12}(t) = F_{ij,st} \frac{N_i^{12}(t)}{N_{i,st}^{12}}, \quad F_{ij}^{14}(t) = F_{ij,st} \frac{N_i^{12}(t) N_i^{14}(t) m_{14}}{N_{i,st}^{12} N_{i,st}^{14} m_{12}} = F_{ij,st} \frac{N_i^{14}(t) m_{14}}{N_{i,st}^{12} m_{12}}$$

Here $F_{ij,st}$ are the steady-state fluxes given in Extended Data Fig. 3 and $m_{12,14}$ is the mass of ^{12,14}C. The fluxes are scaled depending on the deviation from the Holocene steady state $N_{i,st}^{12}$. P_i and $P_{st,i}$ denote the additional and steady state production rate of the *i*th box. The steady state was computed by simulating 200,000 years with the constant production rate $P_{st} = 1.76 \frac{\text{atoms}}{\text{cm}^2 \text{s}}$. The model does not consider any isotopic fractionation and thus the ¹⁴C fluxes scale just as the ¹²C fluxes.

With this a general expression for all boxes at any time can be achieved.

$$\begin{aligned} N(t + \Delta t) &= N(t) + (\Lambda N(t) + F^T(t)\mathbf{1} - F(t)\mathbf{1} + P(t) + P_{st})\Delta t \\ F(t) &= \begin{bmatrix} F^{12}(t) & 0 \\ 0 & F^{14}(t) \end{bmatrix}, \quad \Lambda = \begin{bmatrix} 0 & 0 \\ 0 & -\lambda \end{bmatrix}, \quad N(t) = \begin{pmatrix} N^{12}(t) \\ N^{14}(t) \end{pmatrix}, \quad \mathbf{1}_i = 1 \text{ for all } i \\ P(t) &= Vp(t), \quad P_{st} = Vp_{st} \\ V_i &= \begin{cases} 0.5 \times 0.7, & \text{if } i = \text{index of northern or southern stratosphere} \\ 0.5 \times 0.3, & \text{if } i = \text{index of northern or southern troposphere} \\ 0, & \text{else} \end{cases} \end{aligned}$$

$F^{14}(t)$ and $F^{12}(t)$ are matrices whose components are defined by $F_{ij}^{14}(t)$ and $F_{ij}^{12}(t)$. $F^T(t)$ is the transposed matrix of $F(t)$. Λ is a block matrix where each block is multiplied by a 22 × 22 unit matrix. The Δ^{14} C of each box for the simulation is calculated by the following expression:

$$\Delta^{14}C_i(t) = \frac{\frac{N_i^{14}(t)}{N_i^{12}(t)} - \frac{N_{i,st}^{14}}{N_{i,st}^{12}}}{\frac{N_{i,st}^{14}}{N_{i,st}^{12}}} \times 1,000$$

Where $N_{i,st}^{12,14}$ are the steady-state ^{12,14}C contents of the northern troposphere. By rearranging the differential equation, an expression for the production can be extracted for all times for a given Δ^{14} C data record.

$$p(t) = \frac{\left(\frac{\Delta^{14}C_{\text{Data},i}(t+\Delta t) \frac{N_{i,st}^{14}}{N_{i,st}^{12}} + \frac{N_i^{14}(t)}{N_{i,st}^{12}}}{1000} \right) N_i^{12}(t + \Delta t) - N_i^{14}(t) - (\Lambda N(t) + F^T(t)\mathbf{1} - F(t)\mathbf{1} + P_{st})_i \Delta t}{V_i \Delta t}$$

The $\Delta^{14}\text{C}$ record has to be interpolated to the same resolution as the simulation time step. To do this, the data was linearly interpolated with a monthly sampling. As the differential equation is only solved to first order, the production can only be reconstructed for $\Delta^{14}\text{C}$ records of boxes directly affected by cosmic ray production; namely, the stratosphere or the troposphere. Otherwise, V_i in the denominator would be zero. As our dataset covers atmospheric data recorded by tree rings, this is not an issue. For cases where the reconstructed production rate is negative, the production rate is set to zero. With this model, the ^{14}C production rate can be obtained by calculating the total ^{14}C production needed to reach the next measured $\Delta^{14}\text{C}$ level at each time step. To estimate the uncertainties, a set of 1,000 Monte Carlo simulations was performed, where for each statistical realization of the data, a Savitzky–Golay filter⁵⁷ was applied and the production was reconstructed for the filtered data. The error of the production rate at every time step is given by the standard deviation of all simulations. To get a reasonable start state at a given time, the production rate for the whole IntCal13 record has been calculated and the simulated state can be loaded at any time before AD 1950. The measured data cover a substantial part of the post-industrial era, where anthropogenic carbon emissions need to be considered to correct for the Suess effect³⁰. The Suess effect is a change in the ratio of ^{14}C to ^{12}C caused by the emission of ^{14}C -depleted CO_2 by fossil fuel combustion. For this, the global data of CO_2 emission published by Boden et al.⁵⁸ were used and introduced into the model by increasing the flux between the northern sedimentary sink, which has a ^{14}C to ^{12}C ratio of nearly zero, into the troposphere by the amount given by the data. A reasonable decrease in $\Delta^{14}\text{C}$ matching the observed data is thereby obtained, as can be seen in Extended Data Fig. 4. The interhemispheric offset is also reasonably simulated with a crossing in the correct time period, indicating reasonable interhemispheric exchange rates. With this procedure, the Suess-effect-corrected ^{14}C production can be reconstructed.

Calculation of the solar modulation parameter. The production of radionuclides depends on solar activity and the geomagnetic dipole field in a nonlinear way. To characterize the solar magnetic field we used Φ , which is used to describe the shielding of the cosmic ray flux by solar magnetic activity via the force-field approximation^{23,59}. High Φ values indicate strong solar magnetic shielding, implying a strong deflection of galactic cosmic rays, thus yielding low production rates of cosmogenic nuclides. The reconstruction of solar activity (solar magnetic field) requires variations of the Earth's magnetic field to be considered. For the calculation of Φ , a geomagnetic field record reconstruction by Heliio and Gillet is used⁶⁰, which can be seen in Supplementary Fig. 3 (right), where we chose the covarch_mean record for the reconstruction. The magnetic field strength can be expressed in the form of the virtual axial dipole moment. For a given virtual axial dipole moment and ^{14}C production rate, Φ can be estimated from a look-up table. The relation of the production rate, Φ and the virtual axial dipole moment was computed by Herbst et al.² and is illustrated in Supplementary Fig. 3 (left). The resulting table was calculated by performing a full Monte Carlo simulation of the nucleonic component of the cosmic ray-induced atmospheric cascade². Consequently, the calculation of the solar modulation parameter assumes that all ^{14}C is produced by galactic cosmic rays, where the intensity of galactic cosmic rays outside the heliosphere is assumed to be constant. Other potential causes for ^{14}C production, such as solar proton events, galactic gamma-ray bursts or other potential ^{14}C production processes, were not considered.

Modelling of solar energetic particle events. The potential SEP events were evaluated by using our global carbon model. The relative production increase was calculated by using 1,000 Monte Carlo realizations of the data, where a Gaussian-shaped production spike with a fixed width of less than 1 yr was fitted for each realization and the integrated production was compared to the mean production of the time interval. The results of all of the Monte Carlo simulations for the different datasets of the different events are shown in Extended Data Fig. 6 together with their relative production increases.

Random data generation. Random datasets were generated with a scattering amplitude in the same range as the measurement uncertainties. Afterwards, an artificial sinusoidal signal with a period of 10.43 yr was added with constant amplitude. In Extended Data Fig. 8, the results of the analyses of six different amplitudes of the periodic signal are shown ranging from 0 (white noise) to 3%. The measured data have a normally distributed point-to-point variation (denoted as $\Delta\Delta^{14}\text{C}$) with a sigma of 2.03%. The point-to-point variation of the generated data was matched to the variation of the data by adjusting the individual uncertainty of the random data. As a consequence, the uncertainty of the random data has to decrease with increasing sine amplitude, as an increase in amplitude induces a spread in the point-to-point variation. The six artificial signals containing different amplitudes of a 10.43 yr sinusoidal signal are then band-pass filtered with a period range of 6–18 yr. Finally, peak-to-peak amplitude and period distributions were evaluated and plotted in a histogram as seen in Extended Data Fig. 8. The shapes of both (amplitude and period) distributions were compared to the measured ^{14}C data and a χ^2 analysis was used to find the best fit with the amplitude and period distribution of the measured data. In this way, we were able to detect a periodic signal in the noisy ^{14}C data and to determine its amplitude.

The above analyses were all carried out using a fixed frequency of $1/10.4\text{ yr}^{-1}$ for the artificial sinusoidal signal. A combination of multiple frequencies would probably have been more appropriate for a realistic description of the Schwabe cycle. However, tests using a combination of different frequencies similar to the distribution of frequencies seen in the sunspot numbers showed that the shapes of both the period and amplitude distributions were similar to the single-frequency signal and thus do not have an effect on our findings.

Data availability

The excel data that support the findings of this study are available in PANGAEA at <https://doi.org/10.1594/PANGAEA.921808>. Source data are provided with this paper.

References

- Cuny, H. E. et al. Woody biomass production lags stem-girth increase by over one month in coniferous forests. *Nat. Plants* **1**, 15160 (2015).
- Stuiver, M., Kromer, B., Becker, B. & Ferguson, C. W. Radiocarbon age calibration back to 13,300 Years BP and the ^{14}C age matching of the german oak and united-states bristlecone-pine chronologies. *Radiocarbon* **28**, 969–979 (1986).
- Reimer, P. J. et al. IntCal13 and Marine13 radiocarbon age calibration curves 0–50,000 years cal BP. *Radiocarbon* **55**, 1869–1887 (2013).
- Sookdeo, A. et al. Quality dating: a well-defined protocol implemented at ETH for high-precision ^{14}C dates tested on late glacial wood. *Radiocarbon* <https://doi.org/10.1017/RDC.2019.132> (2020).
- Němec, M., Wacker, L., Hajdas, I. & Gäggeler, H. Alternative methods for cellulose preparation for AMS measurement. *Radiocarbon* **52**, 1358–1370 (2016).
- Welte, C. et al. Towards the limits: analysis of microscale ^{14}C samples using EA-AMS. *Nucl. Instrum. Methods Phys. Res. Sect. B* **437**, 66–74 (2018).
- Wacker, L., Nemeč, M. & Bourquin, J. A revolutionary graphitisation system: fully automated, compact and simple. *Nucl. Instrum. Methods Phys. Res. Sect. B* **268**, 931–934 (2010).
- Wacker, L., Christl, M. & Sýnal, H. A. Bats: a new tool for AMS data reduction. *Nucl. Instrum. Methods Phys. Res. Sect. B* **268**, 976–979 (2010).
- Reimer, P. J., Brown, T. A. & Reimer, W. R. Discussion: reporting and calibration of post-bomb C data. *Radiocarbon* **46**, 1299–1304 (2004).
- Stuiver, M. & Becker, B. High-precision decadal calibration of the radiocarbon time scale, AD 1950–6000 BC. *Radiocarbon* **35**, 35–65 (2016).
- Stuiver, M. A note on single-year calibration of the radiocarbon time scale, AD 1510–1954. *Radiocarbon* **35**, 67–72 (1993).
- Stuiver, M., Braziunas, T. F., Becker, B. & Kromer, B. Climatic, solar, oceanic, and geomagnetic influences on late-glacial and holocene atmospheric $^{14}\text{C}/^{12}\text{C}$ change. *Quat. Res.* **35**, 1–24 (1991).
- Stuiver, M. & Braziunas, T. F. Anthropogenic and solar components of hemispheric ^{14}C . *Geophys. Res. Lett.* **25**, 329–332 (1998).
- Manning, S. W. et al. Fluctuating radiocarbon offsets observed in the southern Levant and implications for archaeological chronology debates. *Proc. Natl Acad. Sci. USA* **115**, 6141–6146 (2018).
- Mursula, K., Usoskin, I. G. & Kovaltsov, G. A. Reconstructing the long-term cosmic ray intensity: linear relations do not work. *Ann. Geophys.* **21**, 863–867 (2003).
- Owens, M. J., Usoskin, I. & Lockwood, M. Heliospheric modulation of galactic cosmic rays during grand solar minima: past and future variations. *Geophys. Res. Lett.* **39**, L19102 (2012).
- Guttler, D. et al. Rapid increase in cosmogenic ^{14}C in AD 775 measured in New Zealand kauri trees indicates short-lived increase in ^{14}C production spanning both hemispheres. *Earth Planet. Sci. Lett.* **411**, 290–297 (2015).
- Savitzky, A. & Golay, M. J. E. Smoothing and differentiation of data by simplified least squares procedures. *Anal. Chem.* **36**, 1627–1639 (1964).
- Boden, T. A. & Andres, R. J. *Global, Regional, and National Fossil-Fuel CO₂ Emissions* (Carbon Dioxide Information Analysis Center, 2016); https://doi.org/10.3334/CDIAC/00001_V2016
- Usoskin, I. G., Alanko-Huotari, K., Kovaltsov, G. A. & Mursula, K. Heliospheric modulation of cosmic rays: monthly reconstruction for 1951–2004. *J. Geophys. Res.* **110**, A12108 (2005).
- Heliio, G. & Gillet, N. Time-correlation-based regression of the geomagnetic field from archeological and sediment records. *Geophys. J. Int.* **214**, 1585–1607 (2018).

Acknowledgements

We thank A. Arnold and R. Howard of the Nottingham Tree Ring Dating Laboratory for their careful dissection of the samples of English oak, and S. Arnold for her careful sample preparations. S. St George and the University of Minnesota are acknowledged for carefully reviewing the manuscript and for their positive and constructive comments, which considerably improved this study. The Laboratory of Ion Beam Physics is partially funded by its consortium partners PSI, EAWAG and EMPA. N.B. is funded by the Swiss

National Science Foundation (SNSF grant number SNF 197137). I.U. acknowledges support from the Academy of Finland (project number 321882 ESPERA).

Author contributions

L.W., M.C. and N. Brehm designed the study with input from H.-A.S., A.B., C.T. and N. Bleicher. A.B., C.T. and N. Bleicher supplied the annually resolved tree ring samples and are responsible for the documentation of the dendrochronology. Radiocarbon measurements and analyses were performed by S.B., N. Brehm and L.W. The modelling and interpretation of the ^{14}C data to extract the solar modulation was done by N. Brehm, M.C. and L.W. with input from F.A., J.B., B.K., R.M., S.K.S., I.U. and H.-A.S. N. Brehm, M.C. and L.W. wrote the manuscript with input from all co-authors.

Competing interests

The authors declare no competing interests.

Additional information

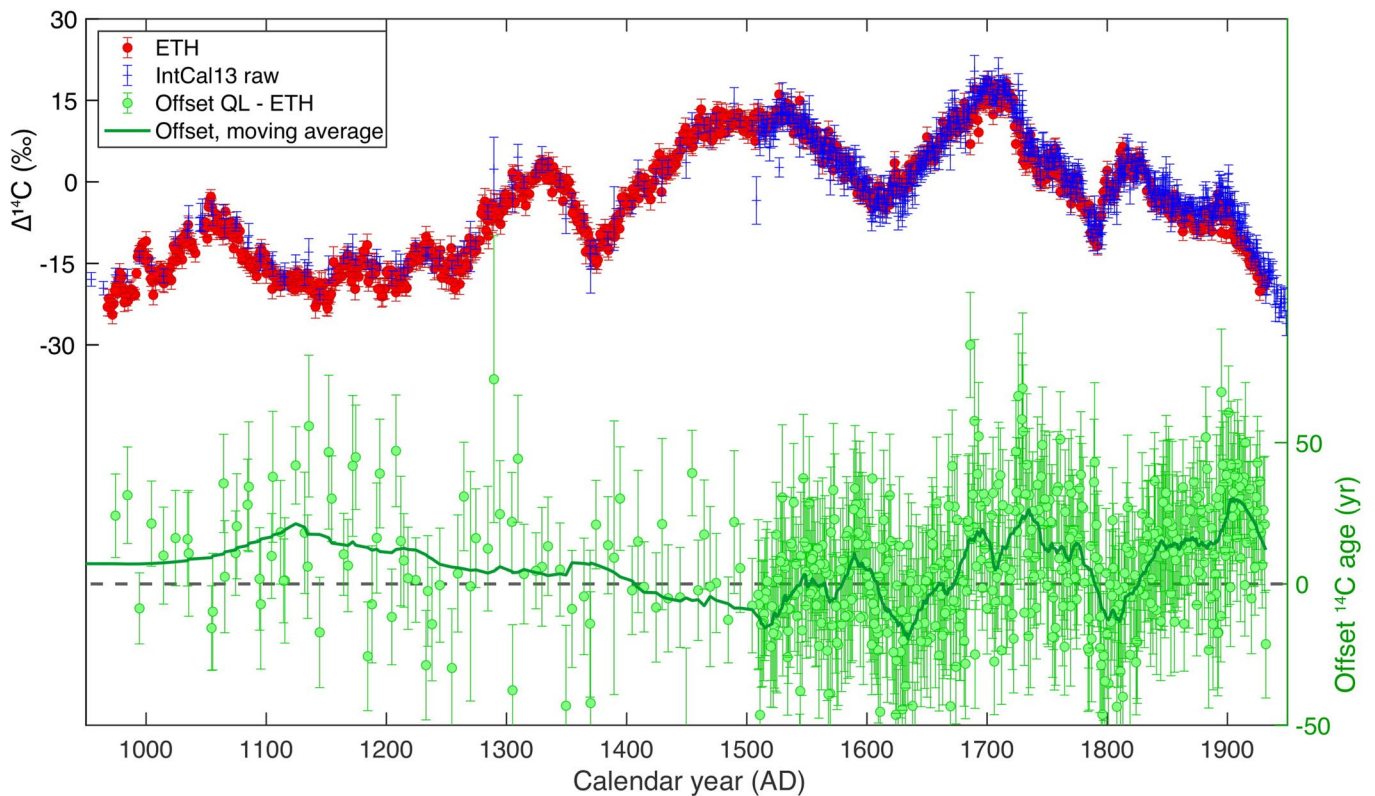
Extended data is available for this paper at <https://doi.org/10.1038/s41561-020-00674-0>.

Supplementary information is available for this paper at <https://doi.org/10.1038/s41561-020-00674-0>.

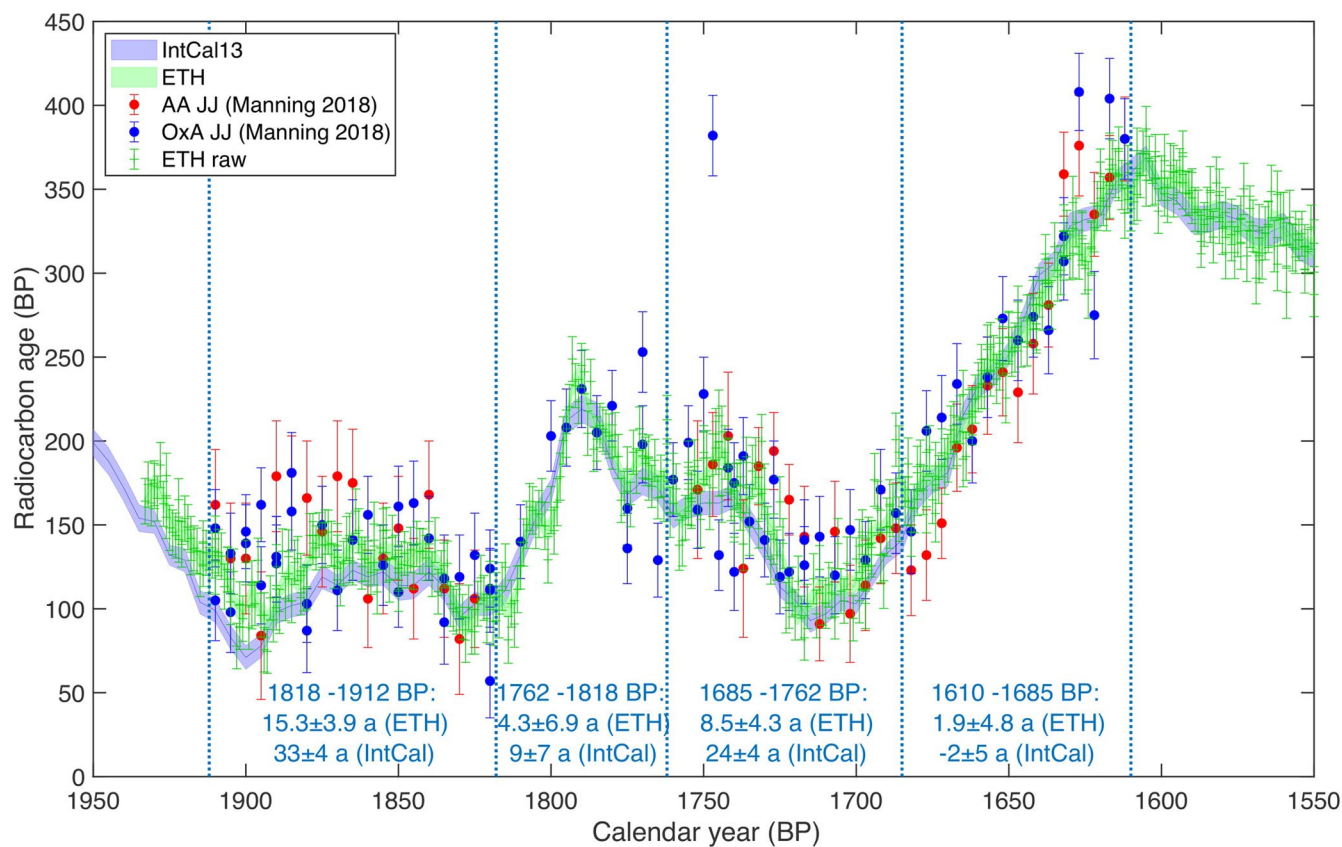
Correspondence and requests for materials should be addressed to N.B., M.C. or L.W.

Peer review information Primary Handling Editor: James Super.

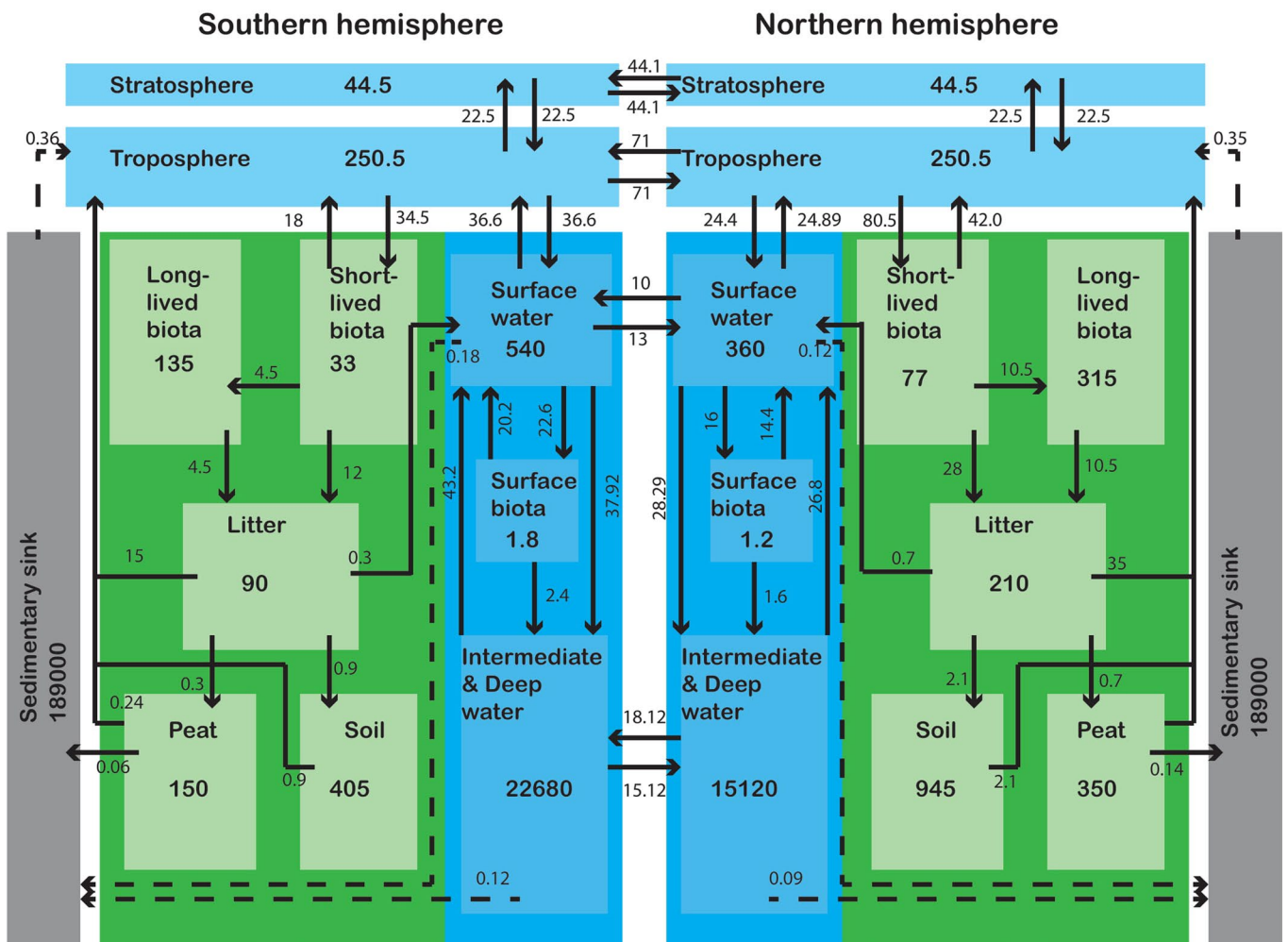
Reprints and permissions information is available at www.nature.com/reprints.



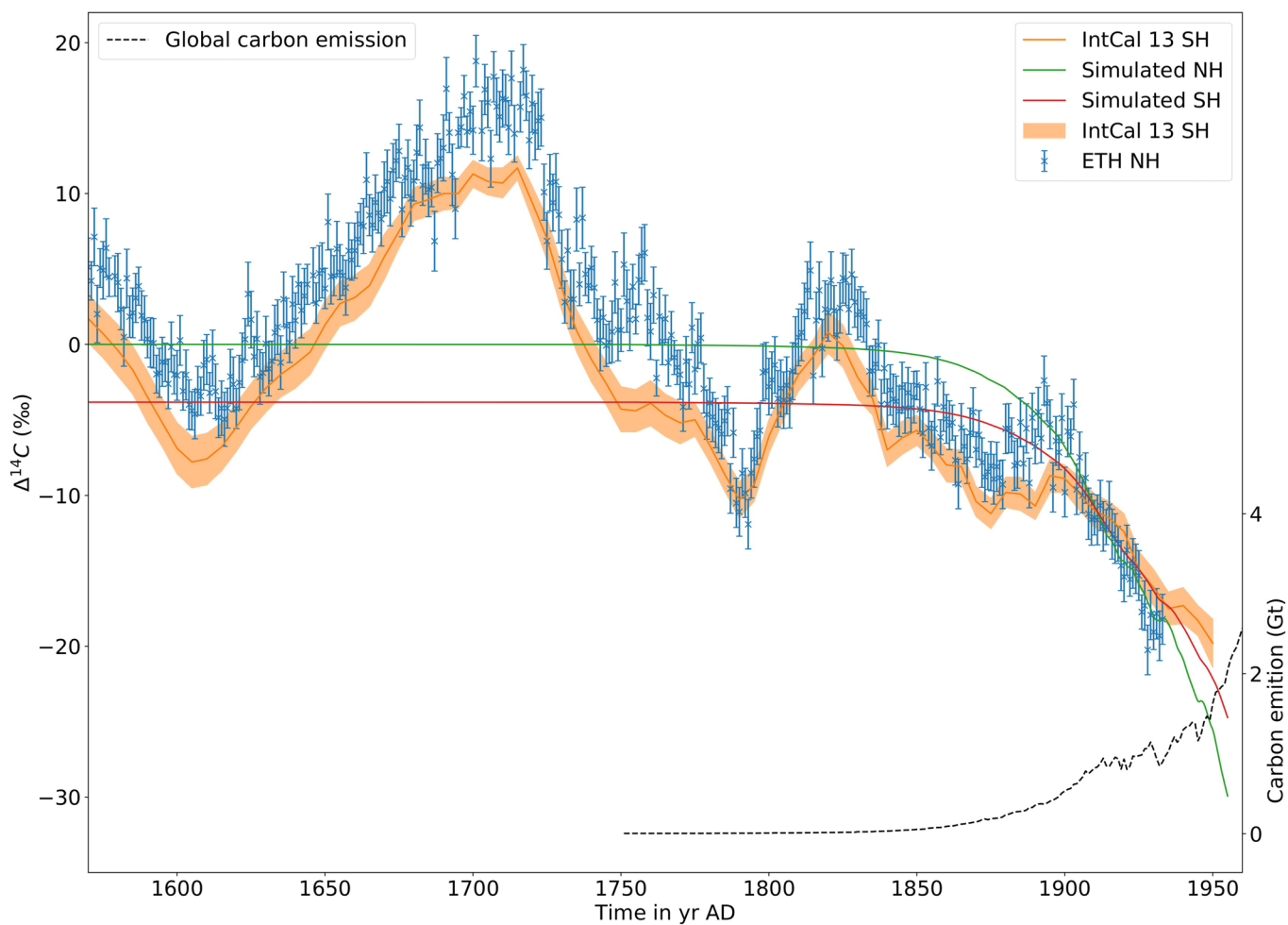
Extended Data Fig 1 | Comparison of IntCal13 raw data with ETH data. Annually resolved radiocarbon measurements as $\Delta^{14}\text{C}$ (red, left axis) compared with the raw data of IntCal13 (blue) at the top. The ^{14}C age offsets in years (QL minus ETH, right axis) of the two datasets (green dots) with a moving average (green line, Savitzky-Golay filter) over time are shown on the bottom (8 years correspond to an offset of 1‰ in $\Delta^{14}\text{C}$). The error bars indicate two sigma errors.



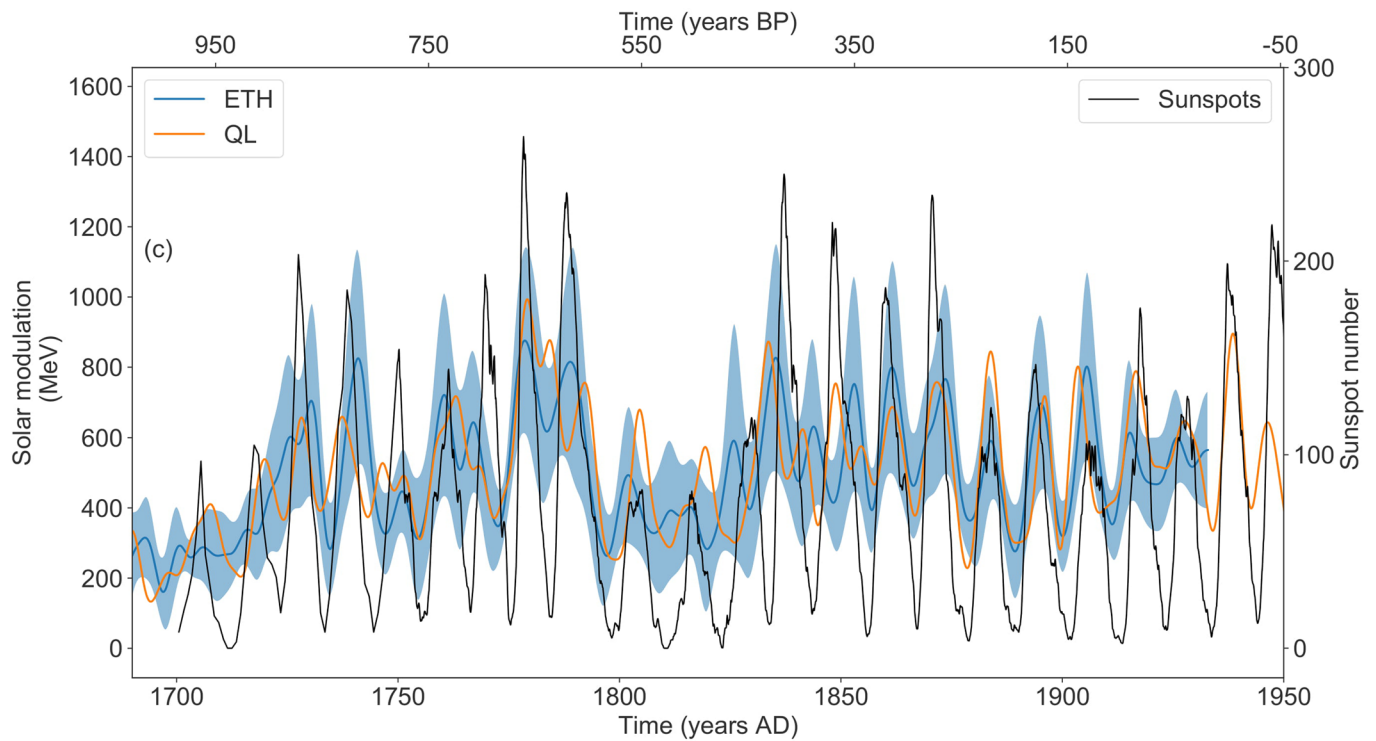
Extended Data Fig 2 | Comparison of Mediterranean Jordanian Juniper data with ETH data. The published radiocarbon measurements on Jordanian juniper (JJ) performed in Oxford (OxA)⁵³ and Arizona (AA)⁵³ are compared with the raw values of IntCal13 (blue curve) and the new annual ETH measurements on British and Swiss oak samples (green) for selected time intervals (between dotted blue lines). The radiocarbon offsets of JJ from IntCal (as already observed by Manning et al.⁵³) are substantially larger in some intervals and less consistent than the offsets of JJ to the ETH data. The error bars indicate two sigma errors.



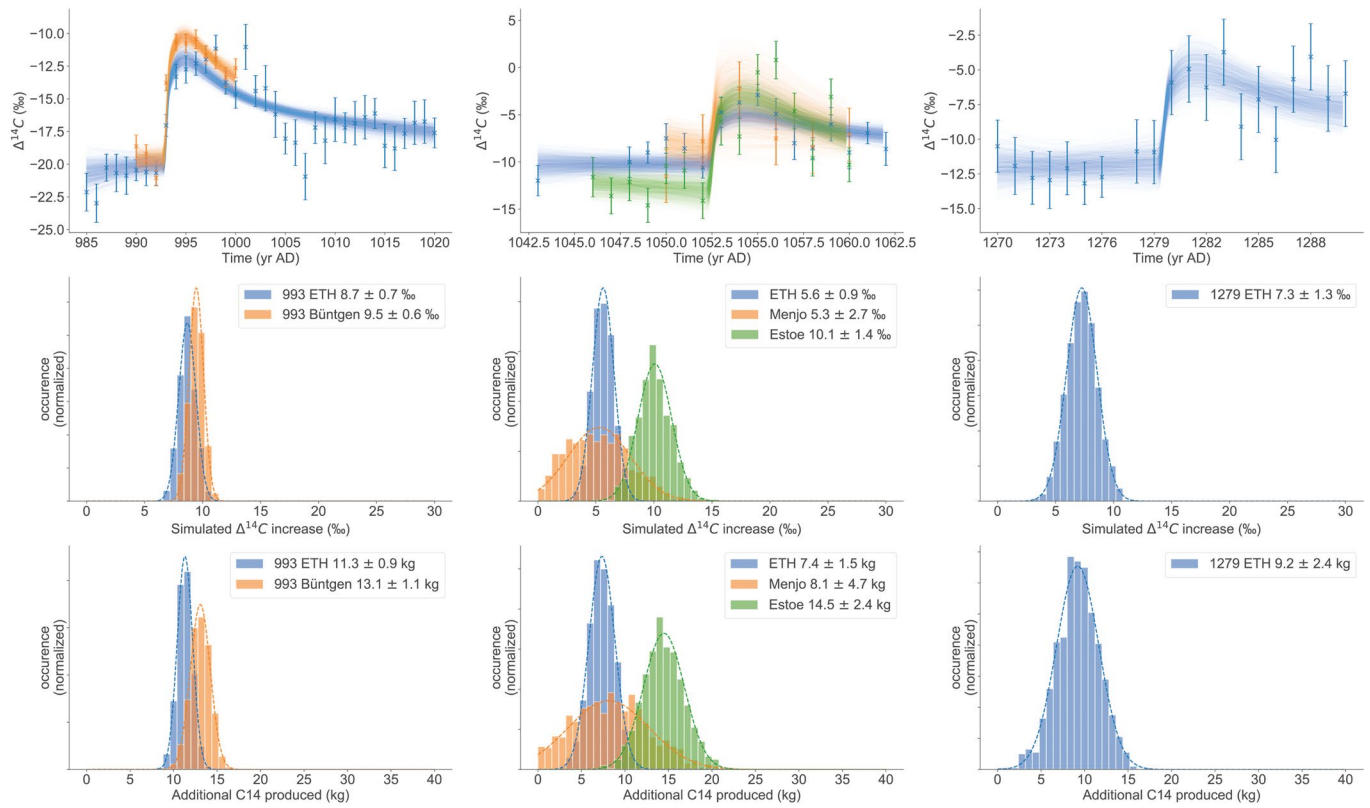
Extended Data Fig. 3 | Depiction of our in-house multi carbon box model. The fluxes are given in Gt/yr and the ¹²C box contents are given in Gt of carbon.



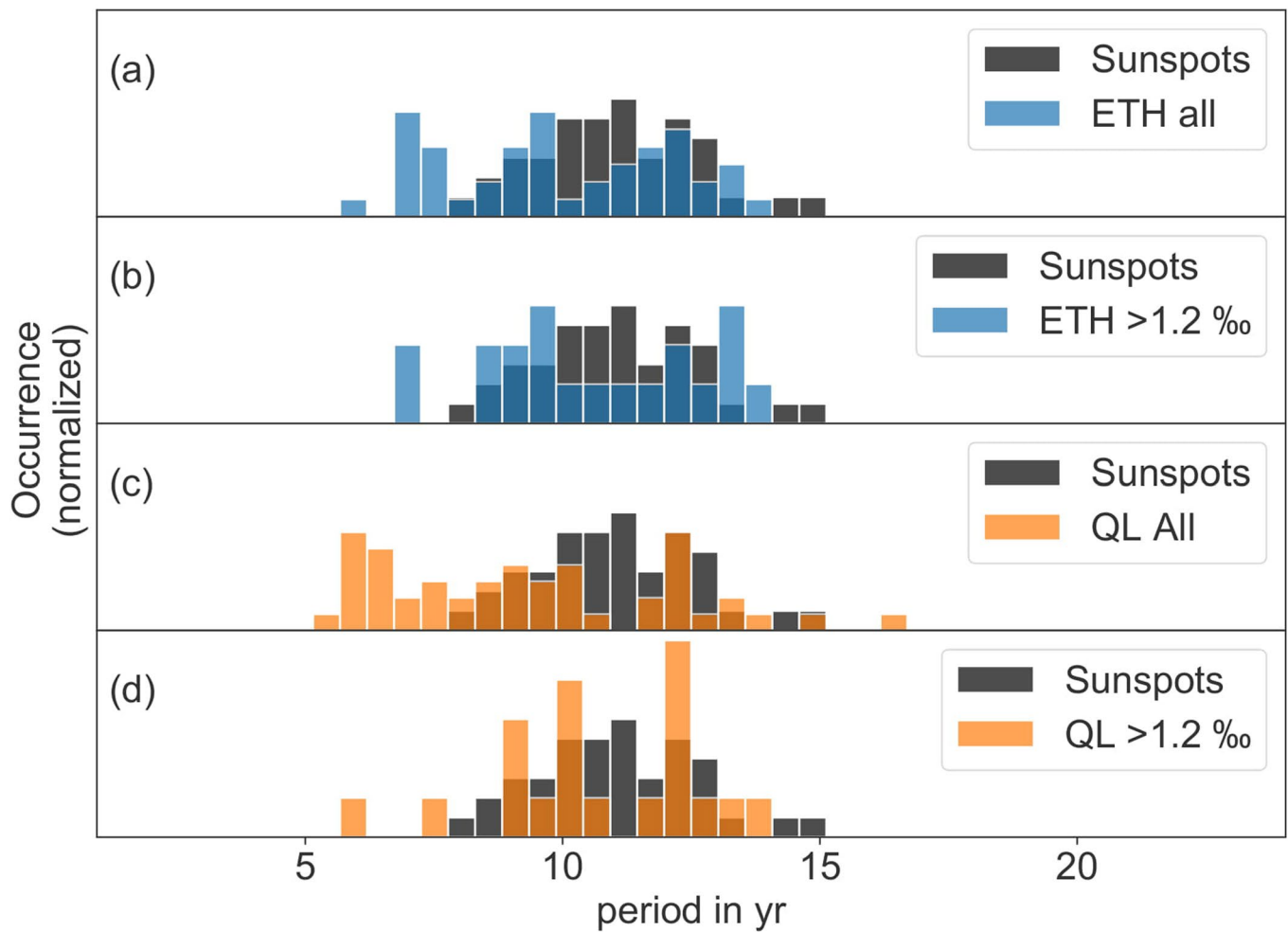
Extended Data Fig. 4 | Simulation of the Suess effect. Simulated decrease of $\Delta^{14}\text{C}$ of the northern (green) and southern (red) hemisphere compared with measured ETH ^{14}C data (blue) and southern hemisphere Intcal13 data⁴² (orange) using a constant ^{14}C production rate of 6.6 kg/yr and using the global emission data of Boden et al.⁵⁸ (black). The error bars indicate two sigma errors.



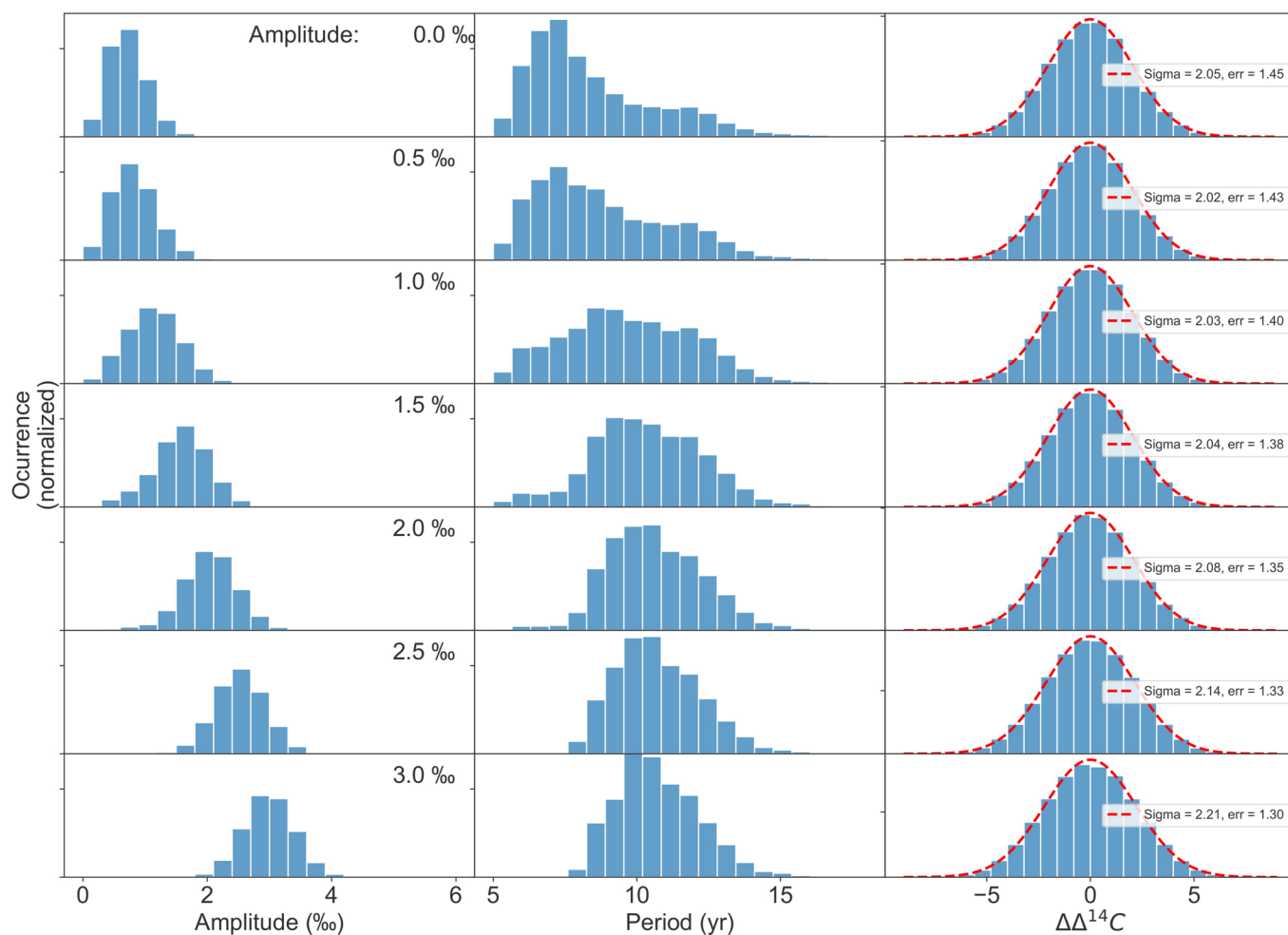
Extended Data Fig. 5 | Direct comparison of reconstructed solar modulation parameter with sunspots. Sunspots³² (black) with the solar modulation parameter calculated from ETH (blue) and QL (orange) data. The blue band indicates the estimated 2 sigma errors of the reconstructed solar modulation parameter of the ETH data by using 1000 Monte Carlo simulations.



Extended Data Fig. 6 | Reconstruction of additionally produced ^{14}C during SEP events. (a) Different Monte Carlo simulations with the distribution in simulated $\Delta^{14}\text{C}$ increases (b) and additional production (c) of the different datasets.



Extended Data Fig. 7 | Direct peak to peak comparison with Sunspots. Comparison of 6–18 yr band passed peak to peak distances of ETH (a/b blue) and QL (c/d orange) with band passed peak to peak distances of sunspots (black). In a/c the histogram of all distances is shown and in b/d only peak distances with a mean amplitude of more than 1.2 ‰ are shown.



Extended Data Fig. 8 | Random data generation with increasing sinusoidal amplitude. The blue histograms show amplitude, period, and point to point distance distributions ($\Delta\Delta^{14}\text{C}$) after 6–18 yr bandpass filtering of random data containing an artificial periodic 10.4 yr signal with different amplitudes. From top to bottom the amplitude of the periodic signal is increased from 0‰ up to 3‰. The artificial data errors were adjusted such that the width of the $\Delta\Delta^{14}\text{C}$ distribution is the same as the $\Delta\Delta^{14}\text{C}$ distribution of our measured samples with a width of 2.03‰.